J|A|C|S
ARTICLES

Published on Web 04/01/2009

$^{15}N-^{15}N$ Proton Assisted Recoupling in Magic Angle Spinning NMR

Józef R. Lewandowski,[†] Gaël De Paëpe,[‡] Matthew T. Eddy, and Robert G. Griffin*

Department of Chemistry and Francis Bitter Magnet Laboratory, Massachusetts Institute of Technology, Cambridge, Massachusetts 02139

Received August 27, 2008; E-mail: rgg@mit.edu

Abstract: We describe a new magic angle spinning (MAS) NMR experiment for obtaining $^{15}N-^{15}N$ correlation spectra. The approach yields direct information about the secondary and tertiary structure of proteins, including identification of α-helical stretches and interstrand connectivity in antiparallel β-sheets, which are of major interest for structural studies of membrane proteins and amyloid fibrils. The method, $^{15}N-^{15}N$ proton assisted recoupling (PAR), relies on a second-order mechanism, third spin assisted recoupling (TSAR), used previously in the context of $^{15}N-^{13}C$ and $^{13}C-^{13}C$ polarization transfer schemes. In comparison to $^{15}N-^{15}N$ proton-driven spin diffusion experiments, the PAR technique accelerates polarization transfer between ^{15}N's by a factor of $\sim 10^2-10^3$ and is furthermore applicable over the entire range of currently available MAS frequencies (10−70 kHz).

1. Introduction

Magic angle spinning (MAS)[1] NMR has emerged as the preferred approach for performing detailed studies of the structure and dynamics of insoluble biological systems and systems lacking long-range order that are currently not accessible by X-ray diffraction or solution NMR. Specifically, MAS experiments are used to investigate protein folding and misfolding, amyloid aggregation, signal transduction, and molecular transport across biomembranes to name a few of the areas of current research[2–13]

A number of developments have contributed to the evolving methodology to determine protein structures via MAS NMR. These include access to high-field magnets (>15 T), improved sample preparation protocols,[14] selective isotopic labeling schemes,[15–18] adaptation of computational protocols for structure calculations,[11,19–22] and new methods for assigning spectra and for measuring distances and torsion angles.[23–43] At present, resonance assignments and structural studies in the solid state

[†] Current address: Université de Lyon, CNRS/ ENS Lyon/ UCB-Lyon 1, Centre RMN à Très Hauts Champs, 5 rue de la Doua, 69100 Villeurbanne, France.

[‡] Current address: INAC/SCIB/LRM, CEA Grenoble, Commissariat à l'énergie Atomique, 17, rue des Martyrs 38054 Grenoble, Cedex 9, France.

(1) Andrew, E. R.; Bradbury, A.; Eades, R. G. *Nature* **1958**, *182*, 1659–1659.
(2) Wasmer, C.; Lange, A.; Van Melckebeke, H.; Siemer, A. B.; Riek, R.; Meier, B. H. *Science* **2008**, *319*, 1523–1526.
(3) Andronesi, O. C.; Becker, S.; Seidel, K.; Heise, H.; Young, H. S.; Baldus, M. *J. Am. Chem. Soc.* **2005**, *127*, 12965–12974.
(4) Franks, W. T.; Wylie, B. J.; Schmidt, H. L. F.; Nieuwkoop, A. J.; Mayrhofer, R. M.; Shah, G. J.; Graesser, D. T.; Rienstra, C. M. *Proc. Natl. Acad. Sci. U.S.A.* **2008**, *105*, 4621–4626.
(5) Frericks, H. L.; Zhou, D. H.; Yap, L. L.; Gennis, R. B.; Rienstra, C. M. *J. Biomol. NMR* **2006**, *36*, 55–71.
(6) Helmus, J. J.; Surewicz, K.; Nadaud, P. S.; Surewicz, W. K.; Jaroniec, C. P. *Proc. Natl. Acad. Sci. U.S.A.* **2008**, *105*, 6284–6289.
(7) Lange, A.; Giller, K.; Hornig, S.; Martin-Eauclaire, M. F.; Pongs, O.; Becker, S.; Baldus, M. *Nature* **2006**, *440*, 959–962.
(8) Petkova, A. T.; Ishii, Y.; Tycko, R. *Biophys. J.* **2002**, *82*, 320A–320A.
(9) Thompson, L. K.; Mcdermott, A. E.; Raap, J.; Vanderwielen, C. M.; Lugtenburg, J.; Herzfeld, J.; Griffin, R. G. *Biochemistry* **1992**, *31*, 7931–7938.
(10) Yang, J.; Paramasivan, S.; Marulanda, D.; Cataidi, M.; Tasayco, M. L.; Polenova, T. *Magn. Reson. Chem.* **2007**, *45*, S73−S83.
(11) Loquet, A.; Bardiaux, B.; Gardiennet, C.; Blanchet, C.; Baldus, M.; Nilges, M.; Malliavin, T.; Boeckmann, A. *J. Am. Chem. Soc.* **2008**, *130*, 3579–3589.
(12) Creuzet, F.; Mcdermott, A.; Gebhard, R.; Vanderhoef, K.; Spijkerassink, M. B.; Herzfeld, J.; Lugtenburg, J.; Levitt, M. H.; Griffin, R. G. *Science* **1991**, *251*, 783–786.
(13) Hong, M. *J. Am. Chem. Soc.* **2000**, *122*, 3762–3770.
(14) Martin, R. W.; Zilm, K. W. *J. Magn. Reson.* **2003**, *165*, 162–174.
(15) Lemaster, D. M. *Prog. Nucl. Magn. Reson. Spectrosc.* **1994**, *26*, 371–419.
(16) LeMaster, D. M.; Kushlan, D. M. *J. Am. Chem. Soc.* **1996**, *118*, 9255–9264.
(17) Goldbourt, A.; Day, L. A.; McDermott, A. E. *J. Magn. Reson.* **2007**, *189*, 157–165.
(18) Hong, M.; Jakes, K. *J. Biomol. NMR* **1999**, *14*, 71–74.
(19) Linge, J. P.; Habeck, M.; Rieping, W.; Nilges, M. *Bioinformatics* **2003**, *19*, 315–316.
(20) Castellani, F.; van Rossum, B.; Diehl, A.; Schubert, M.; Rehbein, K.; Oschkinat, H. *Nature* **2002**, *420*, 98–102.
(21) Manolikas, T.; Herrmann, T.; Meier, B. H. *J. Am. Chem. Soc.* **2008**, *130*, 3959–3966.
(22) Zech, S. G.; Wand, A. J.; McDermott, A. E. *J. Am. Chem. Soc.* **2005**, *127*, 8618–8626.
(23) Bennett, A. E.; Ok, J. H.; Griffin, R. G.; Vega, S. *J. Chem. Phys.* **1992**, *96*, 8624–8627.
(24) Bennett, A. E.; Rienstra, C. M.; Auger, M.; Lakshmi, K. V.; Griffin, R. G. *J. Chem. Phys.* **1995**, *103*, 6951–6958.
(25) Caravatti, P.; Braunschweiler, L.; Ernst, R. R. *Chem. Phys. Lett.* **1983**, *100*, 305–310.
(26) De Paepe, G.; Bayro, M. J.; Lewandowski, J.; Griffin, R. G. *J. Am. Chem. Soc.* **2006**, *128*, 1776–1777.
(27) De Paepe, G.; Elena, B.; Emsley, L. *J. Chem. Phys.* **2004**, *121*, 3165–3180.
(28) De Paepe, G.; Hodgkinson, P.; Emsley, L. *Chem. Phys. Lett.* **2003**, *376*, 259–267.
(29) De Paepe, G.; Lewandowski, J.; Locquet, A.; Bockmann, A.; Griffin, R. G. *J. Chem. Phys.* **2008**, *129*, 1–21.
(30) De Paepe, G.; Lewandowski, J. R.; Griffin, R. G. *J. Chem. Phys.* **2008**, *128*, 124503–26.
(31) Jaroniec, C. P.; Filip, C.; Griffin, R. G. *J. Am. Chem. Soc.* **2002**, *124*, 10728–10742.

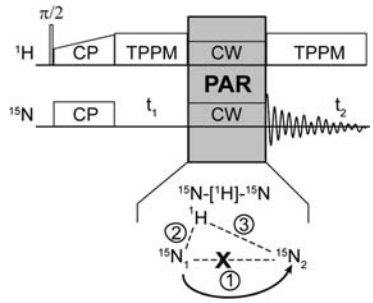

Figure 1. Pulse sequence for the 2D $^{15}N-^{15}N$ PAR correlation experiment. The PAR mixing period consists of C.W. irradiations on the ^{1}H and ^{15}N channels. The irradiation strengths are chosen to produce an appreciable second order TSAR mechanism between the $^{1}H-^{15}N_1$ and $^{1}H-^{15}N_2$ dipolar couplings (terms two and three in the spin system graphics), resulting in TSAR terms of the form $H_zN_1^{\pm}N_2^{\pm}$.

rely mainly on multidimensional $^{13}C-^{13}C$ and $^{15}N-^{13}C-(^{13}C)$ correlation experiments. In addition, $^{15}N-^{15}N$ correlation spectra, which were first reported by Reif, et al. almost a decade ago,[44] are a valuable tool for estimating $^{15}N-^{15}N$ distances[45] and for measuring the NH_i-NH_{i+1} projection angle $\theta_{i,i+1}$,[44,46] To date, however, these experiments have been limited to $B_0 <$ 11−13 T and $\omega_r/2\pi <$ 12 kHz and therefore have not achieved their full potential.

In this paper, we show that $^{15}N-^{15}N$ correlation spectroscopy can be extended to MAS frequencies >15 kHz and to magnetic fields >20 T using the $^{15}N-^{15}N$ proton-assisted recoupling (PAR) technique[29] that was recently introduced in the context of $^{13}C-^{13}C$ and $^{13}C-^{15}N$ recoupling and which relies on a more general third spin assisted recoupling (TSAR) mechanism.[29,41]

We apply the $^{15}N-^{15}N$ PAR pulse sequence (see Figure 1) to a model tripeptide N-*f*-MLF-OH and to the 56-residue microcrystalline β1 immunoglobulin binding domain of protein G (GB1). The mixing time required for observing structurally relevant $^{15}N-^{15}N$ contacts (∼2.8−4.5 A) in the PAR experiment corresponds to tens of milliseconds, improving on spin-diffusion-based techniques (PDSD,[47] DARR[39]) by 2−3 orders of magnitude. In addition, the observed cross-peak intensities can be related to the topology of the $^{15}N-^{15}N$ network in a straightforward manner, thus allowing protein secondary and tertiary structure to be clearly established.

2. $^{15}N-^{15}N$ Correlation Spectroscopy

Despite its low gyromagnetic ratio, ^{15}N has been a valuable nucleus for biomolecular MAS SSNMR studies. Metabolic sources of ^{15}N are relatively inexpensive, allowing one, for example, to prepare uniformly ^{15}N-labeled proteins to screen sample preparation conditions.[14] In addition, an ^{15}N dimension

(32) Jaroniec, C. P.; Tounge, B. A.; Herzfeld, J.; Griffin, R. G. *J. Am. Chem. Soc.* **2001**, *123*, 3507–3519.
(33) Maricq, M. M.; Waugh, J. S. *J. Chem. Phys.* **1979**, *70*, 3300–3316.
(34) Nielsen, N. C.; Bildsoe, H.; Jakobsen, H. J.; Levitt, M. H. *J. Chem. Phys.* **1994**, *101*, 1805–1812.
(35) Oas, T. G.; Griffin, R. G.; Levitt, M. H. *J. Chem. Phys.* **1988**, *89*, 692–695.
(36) Raleigh, D. P.; Levitt, M. H.; Griffin, R. G. *Chem. Phys. Lett.* **1988**, *146*, 71–76.
(37) Schaefer, J.; Mckay, R. A.; Stejskal, E. O. *J. Magn. Reson.* **1979**, *34*, 443–447.
(38) Stejskal, E. O.; Schaefer, J.; Waugh, J. S. *J. Magn. Reson.* **1977**, *28*, 105–112.
(39) Takegoshi, K.; Nakamura, S.; Terao, T. *Chem. Phys. Lett.* **2001**, *344*, 631–637.
(40) Bayro, M. J.; Ramachandran, R.; Caporini, M. A.; Eddy, M. T.; Griffin, R. G. *J. Chem. Phys.* **2008**, 128.
(41) Lewandowski, J. R.; De Paepe, G.; Griffin, R. G. *J. Am. Chem. Soc.* **2007**, *129*, 728–729.
(42) Ramachandran, R.; Lewandowski, J. R.; van der Wel, P. C. A.; Griffin, R. G. *J. Chem. Phys.* **2006**, 124.
(43) Lewandowski, J. R.; De Paepe, G.; van der Wel, P. C. A.; Birkett, N. R.; Belenky, M.; Maly, T.; Bayro, M. J.; Sivertsen, A. C.; Dobson, C. M.; Herzfeld, J.; Griffin, R. G. Submitted for publication, 2008.
(44) Reif, B.; Hohwy, M.; Jaroniec, C. P.; Rienstra, C. M.; Griffin, R. G. *J. Magn. Reson.* **2000**, *145*, 132–141.
(45) Castellani, F. Freien Universität, Berlin, 2003.
(46) Franks, W. T.; Wylie, B. J.; Stellfox, S. A.; Rienstra, C. M. *J. Am. Chem. Soc.* **2006**, *128*, 3154–3155.
(47) Szeverenyi, N. M.; Sullivan, M. J.; Maciel, G. E. *J. Magn. Reson.* **1982**, *47*, 462–475.
(48) Baldus, M. *Prog. Nucl. Magn. Reson. Spectrosc.* **2002**, *41*, 1–47.
(49) Baldus, M.; Geurts, D. G.; Hediger, S.; Meier, B. H. *J. Magn. Reson. Ser. A* **1996**, *118*, 140–144.
(50) Castellani, F.; van Rossum, B. J.; Diehl, A.; Rehbein, K.; Oschkinat, H. *Biochemistry* **2003**, *42*, 11476–11483.
(51) Detken, A.; Hardy, E. H.; Ernst, M.; Kainosho, M.; Kawakami, T.; Aimoto, S.; Meier, B. H. *J. Biomol. NMR* **2001**, *20*, 203–221.
(52) Heise, H.; Seidel, K.; Etzkorn, M.; Becker, S.; Baldus, M. *J. Magn. Reson.* **2005**, *173*, 64–74.
(53) Marulanda, D.; Tasayco, M. L.; Cataldi, M.; Arriaran, V.; Polenova, T. *J. Magn. Reson.* **2005**, *109*, 18135–18145.
(54) Pauli, J.; Baldus, M.; van Rossum, B.; de Groot, H.; Oschkinat, H. *Chembiochem* **2001**, *2*, 272–281.
(55) Rienstra, C. M.; Hohwy, M.; Hong, M.; Griffin, R. G. *J. Am. Chem. Soc.* **2000**, *122*, 10979–10990.
(56) Sun, B. Q.; Rienstra, C. M.; Costa, P. R.; Williamson, J. R.; Griffin, R. G. *J. Am. Chem. Soc.* **1997**, *119*, 8540–8546.
(57) Baldus, M.; Petkova, A. T.; Herzfeld, J.; Griffin, R. G. *Mol. Phys.* **1998**, *95*, 1197–1207.
(58) Caravatti, P.; Bodenhausen, G.; Ernst, R. R. *Chem. Phys. Lett.* **1982**, *89*, 363–367.
(59) Egorova-Zachernyuk, T. A.; Hollander, J.; Fraser, N.; Gast, P.; Hoff, A. J.; Cogdell, R.; de Groot, H. J. M.; Baldus, M. *J. Biomol. NMR* **2001**, *19*, 243–253.
(60) Hong, M.; Griffin, R. G. *J. Am. Chem. Soc.* **1998**, *120*, 7113–7114.
(61) van der Wel, P. C. A.; Lewandowski, J. R.; Griffin, R. G. *J. Am. Chem. Soc.* **2007**, *129*, 5117–5130.
(62) Hong, M.; Gross, J. D.; Griffin, R. G. *J. Magn. Reson.* **1997**, *101*, 5869–5874.
(63) Hong, M.; Gross, J. D.; Hu, W.; Griffin, R. G. *J. Magn. Reson.* **1998**, *135*, 169–177.
(64) Ladizhansky, V.; Jaroniec, C. P.; Diehl, A.; Oschkinat, H.; Griffin, R. G. *J. Am. Chem. Soc.* **2003**, *125*, 6827–6833.
(65) Ladizhansky, V.; Veshtort, M.; Griffin, R. G. *J. Magn. Reson.* **2002**, *154*, 317–324.
(66) Jaroniec, C. P.; MacPhee, C. E.; Astrof, N. S.; Dobson, C. M.; Griffin, R. G *Proc. Natl. Acad. Sci. U.S.A.* **2002**, *99*, 16748–16753.
(67) Jaroniec, C. P.; MacPhee, C. E.; Bajaj, V. S.; Dobson, C. M.; Griffin, R. G. *Biophys. J.* **2003**, *84*, 154A–154A.
(68) Jaroniec, C. P.; MacPhee, C. E.; Bajaj, V. S.; McMahon, M. T.; Dobson, C. M.; Griffin, R. G. *Proc. Natl. Acad. Sci. U.S.A.* **2004**, *101*, 711–716.
(69) Jaroniec, C. P.; Tounge, B. A.; Herzfeld, J.; Griffin, R. G. *Biophys. J.* **2001**, *80*, 368A–368A.
(70) Jaroniec, C. P.; Tounge, B. A.; Rienstra, C. M.; Herzfeld, J.; Griffin, R. G. *J. Am. Chem. Soc.* **1999**, *121*, 10237–10238.
(71) Jaroniec, C. P.; Tounge, B. A.; Rienstra, C. M.; Herzfeld, J.; Griffin, R. G. *J. Magn. Reson.* **2000**, *146*, 132–139.
(72) Rienstra, C. M.; Tucker-Kellogg, L.; Jaroniec, C. P.; Hohwy, M.; Reif, B.; McMahon, M. T.; Tidor, B.; Lozano-Perez, T.; Griffin, R. G *Proc. Natl. Acad. Sci. U.S.A.* **2002**, *99*, 10260–10265.
(73) Sein, J.; Giraud, N.; Blackledge, M.; Emsley, L. *J. Magn. Reson.* **2007**, *186*, 26–33.
(74) Giraud, N.; Blackledge, M.; Bockmann, A.; Emsley, L. *J. Magn. Reson.* **2007**, *184*, 51–61.
(75) Giraud, N.; Blackledge, M.; Goldman, M.; Bockmann, A.; Lesage, A.; Penin, F.; Emsley, L. *J. Am. Chem. Soc.* **2005**, *127*, 18190–201.
(76) Chevelkov, V.; Zhuravleva, A. V.; Xue, Y.; Reif, B.; Skrynnikov, N. R. *J. Am. Chem. Soc.* **2007**, *129*, 12594–5.
(77) Barnes, A. B.; De Paepe, G.; van der Wel, P. C. A.; Hu, K. N.; Joo, C. G.; Bajaj, V. S.; Mak-Jurkauskas, M. L.; Sirigiri, J. R.; Herzfeld, J.; Temkin, R. J.; Griffin, R. G. *Appl. Magn. Reson.* **2008**, *34*, 237–263.
(78) Maly, T.; Debelouchina, G. T.; Bajaj, V. S.; Hu, K. N.; Joo, C. G.; Mak-Jurkauskas, M. L.; Sirigiri, J. R.; van der Wel, P. C. A.; Herzfeld, J.; Temkin, R. J.; Griffin, R. G. *J. Chem. Phys.* **2008**, *128*, 052211.

is often incorporated into advanced multidimensional NMR experiments. ^{15}N- and ^{13}C-labeled samples are routinely used for sequential resonance assignments,[25,41,48–61] for measuring torsion angles,[46,62–65] extracting accurate $^{15}N-^{13}C$ distances,[31,32,66–72] and finally for locally probing protein backbone dynamics.[73–76]

The two main challenges for $^{15}N-^{15}N$ correlation spectroscopy in the solid state have been: (1) the poor sensitivity of ^{15}N observed experiments and (2) the relatively restricted range of available methods for transferring magnetization among ^{15}N nuclei. The first issue is currently being addressed by the development of high-field dynamic nuclear polarization (DNP),[77,78] and the combination of spinning frequencies up to ~70 kHz together with ^{1}H-detected experiments.[79] The second issue mentioned above is directly related to the small magnitude of $^{15}N-^{15}N$ couplings, which currently prevents the wide use of advanced first-order recoupling techniques developed for $^{13}C-^{13}C$ polarization transfer and restricts acquisition of $^{15}N-^{15}N$ correlation experiments primarily to proton driven spin diffusion (PDSD)-based experiments.[17,46,74,80,81]

Although $^{15}N-^{15}N$ PDSD experiments are relatively straightforward to perform, they are far from ideal for biomolecular systems requiring high resolution conditions available at high magnetic field strengths ($B_0 > 16$ T) and MAS frequencies ($\omega_r/2\pi > 20$ kHz). Such operating conditions require long mixing times which reduces the polarization transfer efficiency (due to the competition with the relaxation), and more importantly, complicates the interpretation of the $^{15}N-^{15}N$ polarization transfer buildups in terms of distance restraints.[45]

3. $^{15}N-[^{1}H]-^{15}N$ TSAR$-^{15}N-^{15}N$ PAR Experiments

3.1. TSAR Mechanism Principles. The PAR pulse sequence was recently introduced in the context of $^{13}C-^{13}C$ recoupling.[29] Its underlying mechanism relies on a second-order recoupling process referred to as TSAR that was used to develop the heteronuclear PAINCP[41] (proton assisted insensitive nuclei cross polarization) experiment and has led to an understanding of the beneficial effect of applying a small (<0.25 ω_r) ^{1}H irradiation field to improve the double quantum transfer efficiency of CM_pRR (where p ranges from 3.5 to 5).[30] The TSAR mechanism, denoted as B$-$[A]$-$C, relies on three spin operators that connect spins B and C via a cross term involving dipolar couplings with a third assisting spin A (B$-$A and C$-$A dipolar couplings, respectively). In the experiment described here, the $^{15}N-^{15}N$ PAR pulse sequence relies on a $^{15}N-[^{1}H]-^{15}N$ TSAR mechanism based on cross terms involving heteronuclear $^{1}H-^{15}N_1$ and $^{1}H-^{15}N_2$ dipolar couplings (see inset of Figure 1) to induce polarization transfer between the nitrogen nuclei. As pointed out in our previous work,[29,41] the polarization transfer does not rely on the BC coupling ($^{15}N-^{15}N$ in the experiments described here).

3.2. PAR Pulse Sequence and Effective Hamiltonian. The $^{15}N-^{15}N$ PAR pulse sequence is illustrated in Figure 1 and consists of simultaneous C.W. irradiation on the ^{1}H and ^{15}N channels.

The spin dynamics during the TSAR mixing period can be described by the following Hamiltonian:

$$H = \Delta\omega_{N_1}N_{1z} + \Delta\omega_{N_2}N_{2z} + \Delta\omega_H H_z + \omega_{N_1N_2}[2N_{1z}N_{2z} - (N_{1x}N_{2x} + N_{1y}N_{2y})] + \omega_{N_1H}2N_{1z}H_z + \omega_{HN_2}2H_zN_{2z} + \omega_{1N}(N_{1X} + N_{2X}) + \omega_{1H}H_X \quad (1)$$

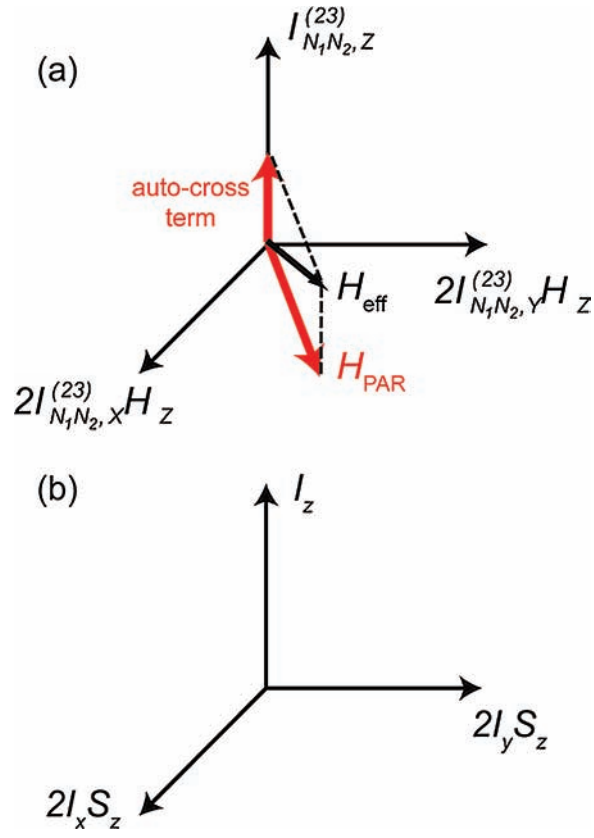

Figure 2. Visualization of the PAR subspace. The space can be seen as a coupled basis between a fictitious ZQ operator involving the two nitrogens (or carbons) and a proton spin. The red arrows indicate PAR recoupling axis and longitudinal tilting field resulting from autocross terms. Panel (b) depicts the coupled basis encountered in solution NMR.

where $\Delta\omega_{N_1}$, $\Delta\omega_{N_2}$, and $\Delta\omega_H$ denote the shift tensors and resonant offsets of the ^{15}N and ^{1}H nuclei respectively, and $\omega_{N_1N_2}$, ω_{N_1H}, and ω_{N_2H} are the homonuclear and heteronuclear dipolar couplings. The last two terms in eq 1 denote the rf fields applied at the ^{15}N and ^{1}H frequencies, respectively. Note that MAS induces a time dependence of the spatial anisotropy of the interactions.

As described in detail by De Paëpe, et al.,[29] an effective TSAR Hamiltonian can be derived in the interaction frame described by the two C.W. rf fields of strength $\omega_{1N}/2\pi$ and $\omega_{1H}/2\pi$ for the ^{15}N and ^{1}H channels. The TSAR subspace (see Figure 2) associated with the polarization transfer is defined by the following operators: $2I^{(23)}_{N_1N_2,X}H_Z$, $2I^{(23)}_{N_1N_2,Y}H_Z$, $I^{(23)}_{N_1N_2,Z}$, which represent a coupled basis between a fictitious ZQ spin (associated with spins N_1 and N_2) and a proton spin H. The TSAR cross term resulting from terms 2 and 3 ($^{1}H-^{15}N_1$ and $^{1}H-^{15}N_2$) in eq 1 can be written in the transverse plane defined by the operators $2I^{(23)}_{N_1N_2,X}H_Z$ and $2I^{(23)}_{N_1N_2,Y}H_Z$, and leads to polarization transfer between N_1 and N_2. The other important contribution to the spin dynamics comes from autocross terms created by term 2 with itself (i.e., $^{1}H-^{15}N_1$ cross $^{1}H-^{15}N_1$) and term 3 with itself (i.e., $^{1}H-^{15}N_1$ cross $^{1}H-^{15}N_1$) respectively. These autocross terms produce an off-resonance contribution along the $I^{(23)}_{N_1N_2,Z}$ operator in the TSAR subspace, which leads to a tilting of the effective recoupling axis and reduces the TSAR polarization transfer efficiency. Note that similar longitudinal terms also arise from autocross terms involving the chemical shift tensor with itself.[29]

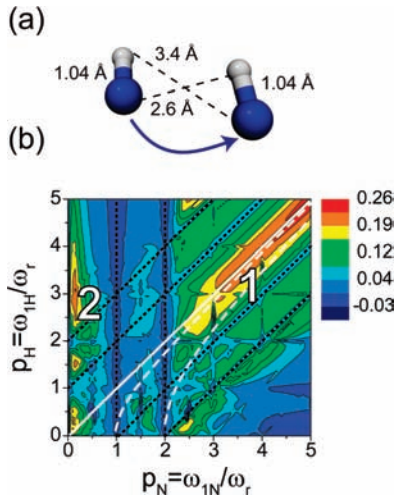

Figure 3. Numerical simulation of a $^{15}N-^{15}N$ PAR polarization transfer map for backbone nitrogens in an α-helix. (a) Spin system used in the simulation consisting of the two backbone nitrogens with directly bonded amide protons (see Table SI1). Simulations were performed at $\omega_r/2\pi = 20$ kHz and $\omega_{0H}/2\pi = 750$ MHz using 20 ms mixing and include typical isotropic and anisotropic chemical shifts (see Table SI1). (b) Contour plot of the $^{15}N-^{15}N$ PAR polarization transfer between neighboring nitrogens in an α-helix as a function of the nitrogen and proton irradiation magnitudes in units of spinning frequency: p_N and p_H. The two main areas used for performing $^{15}N-^{15}N$ PAR experiments are indicated with numerals 1 and 2. The dashed magenta lines indicate conditions for which the $m = 1$ and $m = 2$ components of the autocross term arising from the heteronuclear $^{15}N-^{1}H$ dipolar coupling are zero, respectively. These lines are defined by the following equations: $p_H = (p_N^2 - 1)^{1/2}$ and $p_H = (p_N^2 - 4)^{1/2}$.

3.3. PAR Pulse Sequence Optimization. Figure 3b represents a contour plot of the $^{15}N-^{15}N$ PAR polarization transfer efficiency as a function of the $^{15}N/^{1}H$ rf field strength in units of the spinning frequency (p_N or p_H) for a fixed mixing time of 20 ms. The numerical simulations were performed for $\omega_{0H}/2\pi = 750$ MHz and $\omega_r/2\pi = 20$ kHz with the spin system shown in Figure 3a (corresponding to backbone nitrogens from neighboring residues in an α-helix with the directly attached protons) and include chemical shifts (the atomic coordinates and chemical shift tensors used in the simulations may be found in Table SI1).

The optimization map in Figure 3b displays typical features of PAR polarization transfer.[29] $^{15}N-[^{1}H]-^{15}N$ TSAR polarization transfer is appreciable for settings that avoid first-order recoupling conditions such as ^{15}N rotary resonance (i.e., $p_N = 1, 2$) and $^{1}H-^{15}N$ Hartmann−Hahn conditions (black dotted lines). Indeed, in these cases the $^{15}N-[^{1}H]-^{15}N$ TSAR polarization transfer is absent either because of ^{15}N CSA recoupling or because the ^{15}N magnetization is transferred to ^{1}H's.

The two main regions that lead to appreciable $^{15}N-^{15}N$ polarization transfer are marked on the map with numbers. Area **1** is located under the $p_H = p_N$ condition (white solid line) for $p_N > 2$ and area **2** corresponds to settings where $p_N < 1$ and $p_H > 2$. Note that the first of the above conditions leads to more broadband recoupling than the second area as it employs a higher ^{15}N rf field strength. These favorable settings correspond to conditions where the transverse TSAR term dominates the off-resonance longitudinal term originating from autocross terms. More precisely, each autocross terms is the sum of two contributions involving the $m = 1$ and the $m = 2$ components of the heteronuclear $^{15}N-^{1}H$ dipolar interactions associated with the frequencies ω_r and $2\omega_r$, respectively. The two white dashed lines displayed in Figure 3 represent rf settings where each of these contributions is zero.[29] These lines are defined by the following equations: $p_H = (p_N^2 - 1)^{1/2}$ and $p_H = (p_N^2 - 4)^{1/2}$. The contribution to the autocross terms arising from the $m = 1$ component has a higher scaling factor which explains why one set of the optimal rf settings for the TSAR transfer are found along the $p_H = (p_N^2 - 1)^{1/2}$ lines.

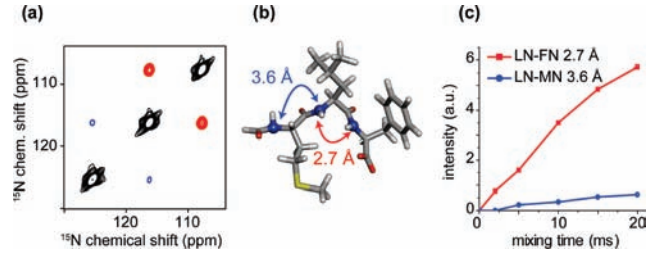

Figure 4. (a) Low-power 2D $^{15}N-^{15}N$ PAR correlation spectrum obtained on $[U-^{13}C,^{15}N]-f$-MLF-OH[72] at $\omega_r/2\pi = 20$ kHz and $\omega_{0H}/2\pi = 900$ MHz using 20 ms of mixing time. The red cross peaks correspond to a short LN-FN sequential contact ($r_{NN} = 2.7$ Å, ∼10% efficiency at 20 ms) and the blue cross peaks correspond to the long sequential LN−MN contact ($r_{NN} = 3.6$ Å, ∼5% efficiency at 20 ms) (see (b)). (c) Cross peak intensity build-ups in $[U-^{13}C,^{15}N]-$N-f-MLF-OH as a function of $^{15}N-^{15}N$ PAR mixing time. The PAR mixing consisted of ∼4 kHz ^{15}N and ∼53 kHz ^{1}H C.W. irradiations for both (a) and (c).

4. PAR Experiments: Application to Peptide and Protein

4.1. $^{15}N-^{15}N$ PAR on N−[U−^{13}C,^{15}N]-f-MLF-OH. Figure 4a shows a 2D $^{15}N-^{15}N$ PAR correlation spectra obtained at $\omega_{0H}/2\pi = 900$ MHz on the tripeptide $N-[U-^{13}C,^{15}N]-f$-MLF-OH using the rf power levels corresponding to area 2—$\omega_{1N}/2\pi \approx 4$ kHz and $\omega_{1H}/2\pi \approx 53$ kHz—with $\omega_r/2\pi = 20$ kHz and $\tau_{mix} = 20$ ms. Note that the low ^{15}N rf power is sufficient to cover the backbone nitrogen bandwidth (∼2.7 kHz at $\omega_{0H}/2\pi = 900$ MHz). Such low power rf settings minimize the rf sample heating, reducing the danger of compromising the sample integrity during the experiment.

At 20 ms mixing time, the spectrum displays two sequential contacts in the tripeptide N-f-MLF-OH corresponding to the $^{15}N-^{15}N$ distances of 2.7 and 3.6 Å, respectively.[72] Although the involved $^{15}N-[^{1}H]-^{15}N$ TSAR recoupling mechanism does not rely on the $^{15}N-^{15}N$ couplings and thus does not directly rely on the $^{15}N-^{15}N$ distances,[29] the strongest cross peak corresponds to the shortest $^{15}N-^{15}N$ distance. This is illustrated in Figure 4c that shows the polarization transfer (under the TSAR settings mentioned above) as a function of the mixing time. In this case, the sequential transfer appears "indirectly" sensitive to the $^{15}N-^{15}N$ distances since the corresponding PAR couplings are proportional to the sequential $^{15}N-^{1}H$ distances.

N-f-MLF-OH is a well-suited model system for testing typical $^{15}N-^{15}N$ sequential spin topologies present in proteins. The LN−FN topology is similar to that encountered for neighboring residues in α-helices (∼2.8 Å $^{15}N-^{15}N$, ∼2.4 and ∼2.8 Å $^{1}H-^{15}N$ distances). On the other hand, the MN−LN arrangement corresponds to neighboring residues in β-sheets (∼3.5 Å $^{15}N-^{15}N$, ∼3.4 and ∼3.9 Å $^{1}H-^{15}N$ distances). In Figure 4 we

(79) Zhou, D. H.; Shea, J. J.; Nieuwkoop, A. J.; Franks, W. T.; Wylie, B. J.; Mullen, C.; Sandoz, D.; Rienstra, C. M. *Angew. Chem., Int. Ed.* **2007**, *46*, 8380–8383.
(80) Marulanda, D.; Tasayco, M. L.; McDermott, A.; Cataldi, M.; Arriaran, V.; Polenova, T. *J. Am. Chem. Soc.* **2004**, *126*, 16608–20.
(81) Seidel, K.; Etzkorn, M.; Heise, H.; Becker, S.; Baldus, M. *Chembiochem* **2005**, *6*, 1638–47.

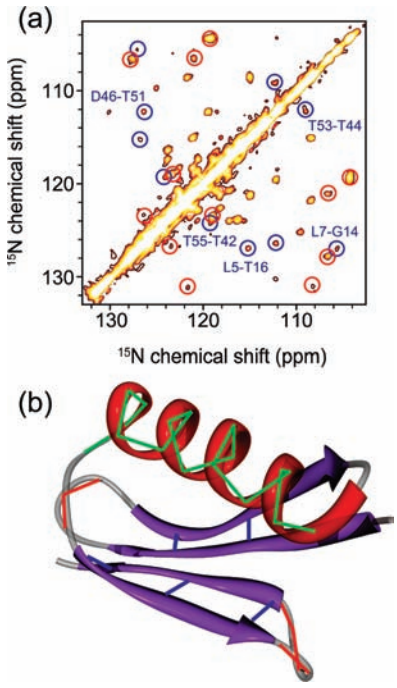

Figure 5. (a) 2D $^{15}N-^{15}N$ PAR correlation spectrum on [1,3-^{13}C, U$-^{15}N$]$-$GB1. The spectrum was obtained using 18 ms PAR mixing with $\omega_{1N}/2\pi \approx 52$ kHz and $\omega_{1H}/2\pi \approx 49$ kHz at $\omega_r/2\pi = 20$ kHz and $\omega_{0H}/2\pi =$ 900 MHz. The cross peaks circled in red correspond to sequential contacts in loop regions that are also indicated with red lines in (b)). The cross peaks circled in blue correspond to contacts between the strands in antiparallel β-sheets (nitrogens for the residues participating in a β-bridge) that are also indicated with blue lines in (b). The unmarked cross peaks correspond primarily to the sequential contacts in the α-helix that are marked with green lines in (b).

can clearly distinguish between these two different topologies simply on the basis of the cross-peak intensity.

4.2. $^{15}N-^{15}N$ PAR on Microcrystalline Protein GB1. Figure 5 shows a 2D $^{15}N-^{15}N$ PAR correlation spectrum on [1,3-^{13}C, U$-^{15}N$] protein GB1 obtained at $\omega_{0H}/2\pi = 900$ MHz and $\omega_r/2\pi = 20$ kHz using 18 ms mixing with $\omega_{1H}/2\pi \approx 49$ kHz and $\omega_{1N}/2\pi \approx 52$ kHz (see Figure SI1 for the spectrum obtained using 22 ms mixing with $\omega_{1N}/2\pi \approx 4$ kHz ^{15}N and $\omega_{1H}/2\pi \approx$ 55 kHz, $\omega_{0H}/2\pi = 900$ MHz and $\omega_r/2\pi = 20$ kHz and Figure SI3 for spectrum obtained using 20 ms mixing with $\omega_{1N}/2\pi \approx$ 71 kHz and $\omega_{1H}/2\pi \approx 69$ kHz at $\omega_{0H}/2\pi = 500$ MHz and $\omega_r/2\pi = 11$ kHz). With this mixing time the spectrum contains two important categories of cross peaks corresponding to the strongest PAR couplings that are well above the noise level (see the cross-peak list in Table SI4). The first contains short ($\leq$3.2 Å) sequential $^{15}N-^{15}N$ contacts (see Table 1), which are primarily observed in α-helical regions and occasionally in loops and turns. The second category consists of $^{15}N-^{15}N$ contacts between residues participating in β-bridges involving antiparallel β-sheets (see Table 1). Note that for these particular settings the sequential cross peaks in the β-sheets are generally weak or below the noise level since the corresponding PAR couplings are not favorable. Indeed, the sequential $^1H-^{15}N$ distances in β-sheets correspond to ~3.8−4.1 Å, whereas the interstrand $^1H-^{15}N$ distances in antiparallel β-sheets are generally smaller (~3.3−3.7 Å). Observation of sequential cross peaks in β-sheets requires longer PAR mixing times and increased signal averaging (see Figure 4).

(82) Zheng, Y.; Yang, D. W. *Bioinformatics* **2005**, *21*, 2925–2926.

These experimental observations can be fully supported by numerical simulations. In the next section we study the relationship between PAR buildups, $^{15}N-^{15}N$ distances and the type of contacts involved.

5. $^{15}N-[^1H]-^{15}N$ PAR Experiments Applied to Structure Determination

The relationship between the TSAR buildups and the internuclear distances is discussed in detail for the case of the $^{13}C-[^1H]-^{13}C$ TSAR mechanism by De Paëpe et al.[29] If only three spins are considered, i.e., two carbons/nitrogens and a single proton, it was shown that the TSAR coupling was proportional to the product of $^{13}C-^1H/^{15}N-^1H$ couplings, independent from the $^{13}C-^{13}C/^{15}N-^{15}N$ distance and strongly dependent on the angle between the heteronuclear interactions involved.[29]

In the case where multiple protons are involved, e.g., fully protonated systems, the TSAR buildup analysis is more complicated, at least analytically. Indeed, the TSAR polarization transfer in this case is the result of the superposition of multiple contributions involving nearby protons (typically protons which are closer than 2.5 Å for the $^{13}C-[^1H]-^{13}C$ case). However, it was found experimentally that the $^{13}C-[^1H]-^{13}C$ buildups recorded on fully protonated [U$-^{13}C$, $^{15}N]-$Crh can, to a large extent, be classified in different distance classes and used to perform a 3D structure calculation.[29]

As we have already mentioned above, the spatial distribution of backbone ^{15}N's and amide ^1H's is intimately linked to the secondary, tertiary, and often quaternary structure of proteins and nucleic acids through the pattern of hydrogen bonds. Table 1 lists $^{15}N-^{15}N$ and important $^1H-^{15}N$ distances in some typical motifs encountered in proteins. Because PAR polarization transfer is proportional to the product of the $^1H-^{15}N$ couplings, it ideally suited for probing geometries imposed by hydrogen bonding patterns. We illustrate this in the next sections where we consider $^{15}N-^{15}N$ PAR polarization transfer in three different typical secondary and tertiary structural motifs encountered in proteins: α-helix, antiparallel β-sheet, and parallel β-sheet.

5.1. Sequential $^{15}N-^{15}N$ Contacts in an α-Helix. Figure 6 shows numerical simulations of the $^{15}N-^{15}N$ polarization transfer in a typical α-helical spin system taken from the X-ray structure of protein GB1 (PDB 2GI9). The spin system is depicted in Figure 6a and consists of four backbone ^{15}N's and amide ^1H's from four consecutive residues in an α-helix. The initial magnetization is placed on $Q_{32}N$ and the polarization transfer to the other ^{15}N's is monitored as a function of time. Note that the distances between amide protons (^1H_n) to sequential nitrogens ($^{15}N_{n\pm1}$) in α-helices are the shortest $^1H-^{15}N$ distances (excluding directly bonded spins) of all the spin topologies presented in Table 1. Consequently, the corresponding $^{15}N-[^1H]-^{15}N$ polarization transfer, simulated in Figure 6b, displays the most rapid (10−20 ms) buildup time and is consistent with the experimental data.

The spin system used in the simulations in Figure 6b includes only the amide protons, so strictly speaking it corresponds to a perdeuterated sample with back-exchanged amide protons. We have shown that in the case of $^{13}C-[^1H]-^{13}C$ TSAR usually multiple protons participate and influence polarization transfer between any two given ^{13}C sites. In order to evaluate the influence of protons other than amide protons we have performed a series of multispin simulations on the α-helix spin system. Figure 6c shows simulations for an α-helix with amide protons and alpha protons (which are, besides the amide ^1H's, consistently the most strongly coupled to

Table 1. Average N−N and H−N Distances in Typical Elements of Secondary Structure in Proteins[a]

type of contact	N_1-N_2 (Å)	N_1-H_2 (Å)	N_2-H_1 (Å)
sequential N_i-N_{i+1} in β-sheet	3.5 ± 0.2	3.9 ± 0.3	3.7 ± 0.7
sequential N_i-N_{i+1} in α-helix	2.8 ± 0.1	3.3 ± 0.1	2.5 ± 0.1
sequential N_i-N_{i+2} in α-helix	4.3 ± 0.1	3.6 ± 0.2	5.0 ± 0.1
sequential N_i-N_{i+3} in α-helix	4.8 ± 0.2	6.8 ± 2.4	7.6 ± 1.8
β-bridge partners in antiparallel β-sheet	4.5 ± 0.4	3.8 ± 0.7	3.8 ± 0.7
β-bridge partners in parallel β-sheet	4.8 ± 0.2	4.0 ± 0.4	5.7 ± 0.5

[a] The values were extracted on the basis of 100 randomly chosen protein structures in the program STARS.[82]

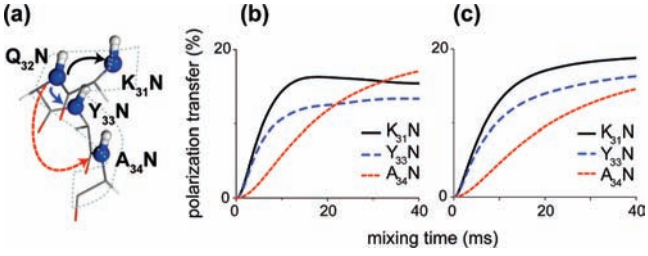

Figure 6. Numerical simulations of $^{15}N-^{15}N$ PAR polarization transfer in an α-helix. The spin system (a) consists of four backbone ^{15}N's and amide ^{1}H's only for simulation in (b) and amide protons plus three Hα's for simulation in (c). The coordinates were taken from residues 31−34 in the X-ray structure of GB1 (PDB 2GI9,[46] see Table SI2). Simulations include nitrogen and proton chemical shifts (see Table SI2). The initial magnetization is placed on $Q_{32}N$. Simulations were performed at $\omega_r/2\pi = 20$ kHz MAS and $\omega_{0H}/2\pi = 750$ MHz with $p_N = 2.7$ and $p_H = 2.5$.

the backbone ^{15}N's). The addition of H_α's only slightly affects the overall polarization transfer with the change more pronounced for N_i-N_{i+2} polarization transfer. This suggest that in order to predict the general trends of $^{15}N-^{15}N$ PAR polarization in proteins we can restrict our analysis to nitrogens and the amide protons (though for a precise analysis requires complex multiple spin simulations).

The simulations in Figure 6 suggest that for mixing times longer than the one we employed in the experiment in Figure 5, we should also observe cross peaks to $N_{n\pm2}$. In fact many $N_i-N_{i\pm2}$ contacts in the helix are also detectable in the data presented in Figure 5 but are much weaker and closer to the noise level.

5.2. $^{15}N-^{15}N$ Contacts in β-Sheets. Figure 7 illustrates numerical simulations of $^{15}N-^{15}N$ polarization transfer in two typical β-sheets geometries: the antiparallel β-sheet arrangement shown in Figure 7a (coordinates from PDB 2GI9)[46] and the parallel β-sheet arrangement shown in Figure 7c (with coordinates taken from the SSNMR structure of the Het-s prion[2]).

The spin system (Figure 7a) used in the simulation in Figure 7b consists of five backbone ^{15}N's in an antiparallel β-sheet with their amide ^{1}H's. In the case of the antiparallel β-sheet arrangement, the interstrand polarization transfer between the β-bridge partners ($T_{44}N$ and $T_{53}N$) is clearly preferred over the transfer to the sequential nitrogens within the strands. Such a situation is a direct consequence of the topology imposed by the hydrogen bonding pattern: the amide protons from the β-bridge partners are pointing toward the nitrogens in the other strand, leading to strong PAR couplings. Moreover, the N_1-H_2 and N_2-H_1 couplings are identical (see Table 1) or very close to each other which results in ideal or close to ideal compensation of the heteronuclear autocross term and consequently no effective tilting of the PAR recoupling axis.

The spin system of Figure 7c consists of five backbone ^{15}N's in a parallel β-sheet and their amide ^{1}H's. The geometry imposed by the hydrogen bonding pattern is not as favorable as in the case of an antiparallel β-sheet for observing interstrand contacts (see also Table 1). In this case the sequential polarization transfer

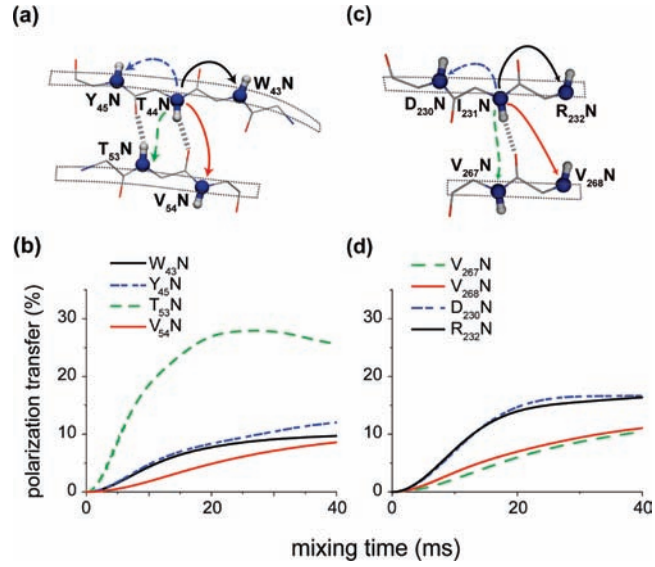

Figure 7. Numerical simulations of $^{15}N-^{15}N$ PAR polarization transfer in an antiparallel β-sheet (a−b) and parallel β-sheet (c−d). In (a) the spin system consists of five backbone nitrogens with directly bonded protons from two strands in an antiparallel β-sheet (coordinates for residues 43−45 and 53−55 from X-ray structure of GB1, PDB 2GI9,[46] see Table SI3). The spin system consists of five backbone nitrogens with directly bonded protons from two strands in a parallel β-sheet (coordinates from SSNMR structure of the HET-s(218−289) prion, PDB 2RNM,[2] see Table SI4). Simulations include nitrogen and proton chemical shifts (see Table SI3 and SI4). The initial magnetization is placed on the $T_{44}N$ in (b) and $I_{231}N$ in (d). Simulations were performed at $\omega_r/2\pi = 20$ kHz MAS and $\omega_{0H}/2\pi = 750$ MHz with $p_N = 2.7$, $p_H = 2.5$.

between the neighboring ^{15}N's is preferred over the polarization transfer between the ^{15}N's in the neighboring strands (which is also consistent with the distribution of NH dipolar couplings in Table 1).

Naturally, the $N_i-N_{i\pm1}$ polarization transfer in both parallel and antiparallel β-sheets have similar characteristics (since the NH couplings for sequential sites are similar, see Table 1), even though overall efficiency of such transfers in the antiparallel β-sheet are lower due to the presence of more favorable transfer between strands.

The simulations suggest $\tau_{mix} \geq 30$ ms for PAR is required for optimal polarization transfer between sequential contacts in β-sheets. This is consistent with our observation of only a few of such cross peaks in the data presented in Figure 5, which uses $\tau_{mix} = 18$ ms.

6. $^{15}N-^{15}N$ PAR in the Context of Other Methods

To complete our discussion, we briefly compare the $^{15}N-^{15}N$ PAR to PDSD and NHHN experiments—two other popular alternatives for $^{15}N-^{15}N$ polarization transfer.

As we have already mentioned above, the $^{15}N-^{15}N$ PAR experiment accelerates the polarization transfer between nitro-

gens by 2−3 orders of magnitude compared to PDSD (milliseconds in PAR versus seconds in PDSD[17,46,74,80,81]). Optimal PDSD mixing times increase with the spinning frequency, rendering it practical for $^{15}N-^{15}N$ correlation experiments employing spinning frequencies $\omega_r/2\pi \leq 12-14$ kHz.[83] For instance, the LN−FN polarization transfer efficiency in the tripetide [U−^{13}C,^{15}N]-*f*-MLF-OH at $\omega_{0H}/2\pi = 750$ MHz drops from 15% to 4% when going from 10 to 20 kHz spinning frequency in an experiment with 2 s of PDSD mixing time. The required increasing PDSD mixing times at higher spinning frequencies also becomes a limiting factor both in terms of loss associated with relaxation and the experimental time per scan. In contrast, according to simulations, $^{15}N-^{15}N$ PAR should be applicable at all spinning frequencies presently accessible in solid-state MAS NMR (up to 70 kHz) requiring reasonable mixing times (on the order of tens of milliseconds).

Moreover, as was shown by Castellani et al.,[45] due to the decreasing overlap integral, the increase of the magnetic field strength adversely affects the polarization transfer in $^{15}N-^{15}N$ PDSD experiment. As a consequence, even though at fields <14 T the correlation between the $^{15}N-^{15}N$ distances and the polarization transfer buildups can be established quite straightforwardly, recovering any such correlation at fields >14 T requires prior knowledge of the undecoupled nitrogen linewidths and correction for the chemical shift differences between the recoupled sites. [45,80]

However, it is important to note that $^{15}N-^{15}N$ PAR and $^{15}N-^{15}N$ PDSD experiments run under optimal conditions provide spectra with quite different information contents and can thus be used jointly.

The NHHN experiment was demonstrated to provide valuable structural information on perdeuterated back-exchanged samples.[84] For example, similarly to the PAR experiment presented here, NHHN yields contacts between strands in antiparallel β-sheets (though the crowding should be reduced in PAR spectra with sequential cross peaks in β-sheets significantly attenuated at mixing times favoring the interstrand polarization transfer). However, it was also noted that the performance of the NHHN experiment deteriorates significantly in fully protonated samples, where mostly sequential cross peaks are retained.[84] It transpires that $^{15}N-^{15}N$ PAR experiment should be more sensitive than the NHHN experiments for probing $^{15}N-^{15}N$ contacts in a fully protonated sample and yield comparable structural information. This is illustrated in Figure 8, which shows a comparison of the polarization transfer between the β-bridge nitrogen partners in an antiparallel β-sheet in NHHN and $^{15}N-^{15}N$ PAR experiments. It turns out that the addition of six closest protons (see Table SI5 for the details on the spin system) leads to substantial reduction of polarization transfer efficiency in the NHHN experiment, but only a few percent reduction of polarization transfer efficiency in the PAR experiment. Note that in general the number of neighboring protons is much larger than the number of protons that we have included in these simulations, which means that the experimental performance of NHHN may actually deteriorate even further. For example, on the [U−^{13}C,^{15}N]-*f*-MLF-OH sample at $\omega_{0H}/2\pi = 750$ MHz and $\omega_r/2\pi = 20$ kHz the LN−FN polarization transfer in a $^{15}N-^{15}N$ PAR experiment is almost 7 times more efficient than in NHHN experiment run under the same set of conditions (see Figure SI6).

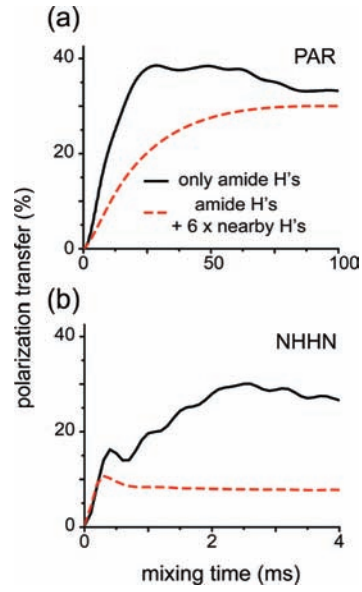

Figure 8. Numerical simulation of PAR (a) and NHHN (b) polarization transfer between nitrogens from a β-bridge partner residues in an antiparallel β-sheet. The black solid line represents simulations with only amide protons included, and the red dashed line represents simulation with amide protons plus six other closest protons. The simulations were performed at $\omega_r/2\pi =$ 20 kHz and $\omega_{0H}/2\pi = 750$ MHz and include all chemical shifts (see Table SI5). The $^1H-^{15}N$ CP steps in NHHN are simulated explicitly using 0.15 ms contact time with $\omega_{1H}/2\pi = 100$ kHz and $\omega_{1N}/2\pi = 80$ kHz. The PAR mixing settings are $p_N = 2.7$ and $p_H = 2.5$.

7. Conclusion

We have described a new experiment for performing $^{15}N-^{15}N$ MAS correlation spectroscopy that provides direct access to secondary and tertiary structural information of proteins. $^{15}N-^{15}N$ PAR accelerates the $^{15}N-^{15}N$ polarization transfer up to 3 orders of magnitude compared to proton-driven spin diffusion experiments. Moreover, in fully protonated samples, $^{15}N-^{15}N$ PAR yields interstrand cross peaks in antiparallel β-sheets, as well as the sequential contacts in helices. Most transmembrane proteins consist of either β-barrel or α-helical structural motifs. Provided that sufficient sensitivity is available, our results suggests that the $^{15}N-^{15}N$ PAR method should allow straightforward identification of α-helical segments and should permit one to establish connectivities between β-strands in β-barrels, which typically consist of antiparallel β-sheets and thus provide valuable structural information about membrane proteins. Moreover, the fact that the interstrand $^{15}N-^{15}N$ contacts for the β-bridge partners in antiparallel β-sheets are substantially larger than sequential $^{15}N-^{15}N$ contacts within the strands should lead to significant simplification of the spectra without need for deuteration or other specific labeling—a feature that should be greatly appreciated in larger systems with significant spectral overlap.

$^{15}N-^{15}N$ PAR is applicable over almost the entire range of MAS frequencies currently available (10−70 kHz) and could be used as a building block for more sophisticated SSNMR experiments. More importantly, $^{15}N-^{15}N$ spectroscopy should

(83) Krushelnitsky, A.; Bräuniger, T.; Reichert, D. *J. Magn. Reson.* **2006**, *182*, 339–342.
(84) Reif, B.; van Rossum, B. J.; Castellani, F.; Rehbein, K.; Diehl, A.; Oschkinat, H. *J. Am. Chem. Soc.* **2003**, *125*, 1488–1489.
(85) Franks, W. T.; Zhou, D. H.; Wylie, B. J.; Money, B. G.; Graesser, D. T.; Frericks, H. L.; Sahota, G.; Rienstra, C. M. *J. Am. Chem. Soc.* **2005**, *127*, 12291–12305.

benefit strongly from the development of sensitivity enhanced techniques like DNP and become an integral part of the SSNMR toolkit for structural characterization of proteins.

8. Material and Methods

8.1. Sample Preparation. 8.1.1. Preparation of N-[U−^{13}C,^{15}N]-*f*-MLF-OH. N-*f*-MLF-OH peptide was obtained by solid-phase peptide synthesis from CS Bio, Inc. (Menlo Park, CA). The peptide was prepared with uniformly ^{13}C- and ^{15}N-labeled amino acids from Cambridge Isotope Laboratories (Andover, MA). The peptide was crystallized from isopropanol and packed in a 2.5 mm Bruker rotor.

8.1.2. Preparation of GB1 Samples. Two labeled samples were prepared for ^{15}N−^{15}N TSAR studies: one [1,3 ^{13}C, U−^{15}N] and one [^{12}C, U−^{15}N]. Samples were prepared according to previously published protocol.[85] *Escherichia coli* BL21 (DE3) cells (Invitrogen) were transformed with the T2Q mutant of GB1. The [1,3 ^{13}C, U−^{15}N] sample was grown in M9 minimal media containing 2.0 g of [1,3-^{13}C] glycerol and 2.0 g of ^{12}C $NaHCO_3$ as the sole carbon sources and 1.0 g of ^{15}N ammonium chloride as the sole nitrogen source; the U−^{15}N sample was prepared in M9 minimal media containing 1.0 g ^{15}N ammonium chloride and 8.0 g of ^{12}C glucose. Protein expression, extractions, and purification were done according to previous studies. Microcrystalline samples were prepared according to ref 85 by dialysis in 50 mM phosphate buffer (pH 5.7) and precipitated with three aliquots of 2:1 MPD/IPA at a protein concentration of 25 mg/mL. One sample containing ∼9−10 mg of [1,3 ^{13}C, U−^{15}N]-labeled protein was centrifuged into a 2.5 mm Bruker rotor, while ∼20 mg of [^{12}C, U−^{15}N] protein was centrifuged into a 4.0 mm Varian rotor. Both rotors were sealed with epoxy to maintain sample hydration levels throughout the studies.

8.2. NMR Spectroscopy. The experiments were carried out using a commercial Bruker spectrometer operating at 900.1 MHz ^{1}H Larmor frequency using a Bruker triple-resonance (HCN) probe equipped with a 2.5 mm spinner module. Spinning frequencies of 20 kHz were used in all experiments and regulated to ±2 Hz with a Bruker spinning frequency controller (Bruker BioSpin, Billerica MA).

The PAR experiment was optimized by matching the interference pattern with the simulated PAR optimum (a comparison of the polarization transfer map and the interference map can be found in the Figure SI2). With an optimization of this kind we take advantage of the fact that the conditions leading to destructive interference of nitrogen polarization (i.e., rotary resonance and ^{1}H−^{15}N Hartmann−Hahn conditions) are also outlined as features in the PAR optimization map. The ^{15}N power was set to ∼52 or ∼4 kHz (i.e., $p_N = 2.6$ or 0.2—the value that leads to appreciable TSAR mechanism in simulations) and ^{1}H rf was scanned through to identify Hartmann−Hahn conditions. ^{1}H rf power leading to minimal interference just under the $n = 0$ condition was used for the first case and just under the $n = 3$ Hartmann−Hahn condition for the second case.

The ^{1}H decoupling during t_1 evolution and acquisition was implemented through optimized 100 kHz TPPM.[24] The recycle delay was 3 s. For the 2D ^{15}N−^{15}N PAR correlation spectrum on [U−^{13}C,^{15}N]-*f*-MLF-OH, acquisition times were 20 ms in t_2 and 12.8 ms in t_1 (64 × 200 μs; spectral width 54.8 ppm) with 4−16 scans per t_1 point. One of the 2D ^{15}N−^{15}N PAR correlation spectrum on [1,3-^{13}C,^{15}N]-GB1 was obtained with 18 ms mixing time using ca. 52 kHz ^{15}N and 49 kHz ^{1}H irradiation; acquisition times were 25.6 ms in t_2 and 16 ms in t_1 (80 × 200 μs spectral width 54.8 ppm) with 224 scans per t_1 point. Second of the 2D ^{15}N−^{15}N PAR correlation spectrum on [1,3-^{13}C,^{15}N]-GB1 was obtained with 22 ms mixing time using ∼4 kHz ^{15}N and ∼55 kHz ^{1}H irradiation; acquisition times were 25.6 ms in t_2 and 16 ms in t_1 (64 × 250 μs spectral width 43.8 ppm) with 96 scans per t_1 point. The temperature was regulated using Bruker BCU-X (target temperature −18 °C, flow 1400 L/h, resulting in a sample temperature between 0 to 5 °C as indicated by the water ^{1}H chemical shift referenced to PEG (3.74 ppm, referenced externally to DSS).[86]

8.3. Numerical Simulations and Data Analysis. Numerical simulations were performed using SPINEVOLUTION 3.3. The NH bonds were set to 1.04 Å for the simulations. For viewing and processing PDB files we used UCSF Chimera (Resource for Biocomputing, Visualization, and Informatics at the University of California, San Francisco) (supported by NIH P41 RR-01081)[87] and DS Visualizer 2.0 (Accelrys). Chimera was also used for producing some of the graphics used in figures. Data were processed using NMRPipe[88] and analyzed in Sparky (T. D. Goddard and D. G. Kneller, University of California).

Acknowledgement. We would like thank Dr. Patrick van der Wel for insightful discussions. We are very grateful to Dr. Mikhail Veshtort for providing the SPINEVOLUTION software that has been used throughout the course of this work. This work was supported by the National Institute of Health Grants No. EB-001960, EB-003151, and EB-002026.

Supporting Information Available: Details of the spin systems used in numerical simulations in the text; supplemental figures; low-power ^{15}N−^{15}N PAR spectrum on GB1; and list of observed cross peaks. This material is available free of charge via the Internet at http://pubs.acs.org.

JA806578Y

(86) Cavanagh, J.; Fairbrother, W. J.; Palmer, A. G.; Skelton, N. J.; Rance, M. *Protein NMR Spectroscopy: Principles and Practice*; Academic Press: New York, 2006.
(87) Pettersen, E. F.; Goddard, T. D.; Huang, C. C.; Couch, G. S.; Greenblatt, D. M.; Meng, E. C.; Ferrin, T. E. *J. Comput. Chem.* **2004**, *25*, 1605–12.
(88) Delaglio, F.; Grzesiek, S.; Vuister, G. W.; Zhu, G.; Pfeifer, J.; Bax, A. *J. Biomol. NMR* **1995**, *6*, 277–93.